CentTracker: a trainable, machine-learning–based tool for large-scale analyses of *Caenorhabditis elegans* germline stem cell mitosis

Réda M. Zellag[a,b], Yifan Zhao[a,†], Vincent Poupart[b], Ramya Singh[a,b], Jean-Claude Labbé[b,c,*], and Abigail R. Gerhold[a,*]

[a]Department of Biology, McGill University, Montréal, QC H2A 1B1, Canada; [b]Institute for Research in Immunology and Cancer (IRIC) and [c]Department of Pathology and Cell Biology, Université de Montréal, Succursale Centre-ville, Montréal, QC H3C 3J7, Canada; [†]Present address: Harvard-MIT Health Sciences and Technology, 77 Massachusetts Avenue, Cambridge, MA 02139

ABSTRACT **Investigating the complex interactions between stem cells and their native environment requires an efficient means to image them in situ. *Caenorhabditis elegans* germline stem cells (GSCs) are distinctly accessible for intravital imaging; however, long-term image acquisition and analysis of dividing GSCs can be technically challenging. Here we present a systematic investigation into the technical factors impacting GSC physiology during live imaging and provide an optimized method for monitoring GSC mitosis under minimally disruptive conditions. We describe CentTracker, an automated and generalizable image analysis tool that uses machine learning to pair mitotic centrosomes and that can extract a variety of mitotic parameters rapidly from large-scale data sets. We employ CentTracker to assess a range of mitotic features in a large GSC data set. We observe spatial clustering of mitoses within the germline tissue but no evidence that subpopulations with distinct mitotic profiles exist within the stem cell pool. We further find biases in GSC spindle orientation relative to the germline's distal–proximal axis and thus the niche. The technical and analytical tools provided herein pave the way for large-scale screening studies of multiple mitotic processes in GSCs dividing in situ, in an intact tissue, in a living animal, under seemingly physiological conditions.**

Monitoring Editor
Diane Lidke
University of New Mexico

Received: Nov 16, 2020
Revised: Jan 4, 2021
Accepted: Jan 19, 2021

INTRODUCTION

Tissue-resident stem cells contribute to tissue development, homeostasis, and repair. To do so, stem cells rely on their ability to self-renew and differentiate into more specialized cells. Their behavior is governed in vivo by a specialized microenvironment, termed the niche, which provides signals that determine stem cell fate. Niche signaling protects against overgrowth or tissue loss, by controlling the size of the stem cell population and preventing inappropriate self-renewal (Weaver and Cleveland, 2005; Lu and Johnston, 2013; Januschke and Näthke, 2014). Accordingly, the interactions in vivo between stem cells, their niche and their tissue of residence are crucial. Live-imaging approaches that permit real-time visualization of stem cells within their natural environment (i.e., intravital imaging) have provided valuable insight into stem cell biology (Park *et al.*, 2016), yet these approaches often remain technically challenging.

Intravital imaging of *Caenorhabditis elegans* germline stem cells (GSCs) provides an opportunity to combine well-established genetic tools with cell biological techniques to elucidate how stem cells are regulated in vivo (Narbonne *et al.*, 2016; Hubbard and Schedl, 2019). *C. elegans* hermaphrodites have two U-shaped, tube-like gonad arms, each organized like an assembly line, with a mitotic zone at the distal end that houses the GSCs (Figure 1A). As

This article was published online ahead of print in MBoC in Press (http://www.molbiolcell.org/cgi/doi/10.1091/mbc.E20-11-0716) on January 27, 2021.

*Address correspondence to: Abigail Gerhold (abigail.gerhold@mcgill.ca) and Jean-Claude Labbé (jc.labbe@umontreal.ca).

Abbreviations used: D/P, distal/proximal; DTC, distal tip cell; GFP, green fluorescent protein; GSC, germline stem cell; mCh, monomeric cherry fluorescent protein; mNG, monomeric neon green fluorescent protein; NEBD, nuclear envelop breakdown; NGM, nematode growth media; PCA, principle component analysis; RNAi, RNA-mediated interference; SAC, spindle assembly checkpoint; TPCF, two point correlation function; VPC, vulval precursor cell.

cells move proximally, they enter meiosis, eventually giving rise to mature gametes, which are found at the most proximal end of each gonad. GSC fate is governed by signaling from a somatic cell, termed the distal tip cell (DTC), that is located at the distal tip of each gonad arm and acts as a niche (Kimble and White, 1981; Crittenden *et al.*, 2006). The DTC uses Notch signaling to regulate whether GSCs remain in an undifferentiated, mitotic state or initiate differentiation by entering meiosis (Hubbard and Schedl, 2019). Like mammalian intestinal stem cells, *C. elegans* GSCs appear to self-renew according to a population model in which GSC losses due to differentiation or damage are compensated by symmetric divisions, thus maintaining a relatively constant number of stem cells (Morrison and Kimble, 2006; Joshi *et al.*, 2010; Rosu and Cohen-Fix, 2017; Hubbard and Schedl, 2019). Because Notch signaling relies on cell–cell interactions, maintaining contact with the niche following division could be a mechanism to control GSC fate (Schofield, 1978; Kimble, 1981; Kimble and Crittenden, 2007; Morrison and Kimble, 2006; Kotak, 2019).

Monitoring GSCs in situ via fluorescence microscopy is facilitated by the fact that *C. elegans* adults are transparent; however, technical challenges remain. Live imaging of dynamic subcellular events requires high temporal and spatial resolution. Notably, *C. elegans* animals are highly active and have relatively small cellular structures (e.g., the nuclei of adult GSCs are 4–5 μm in diameter); thus effective, yet gentle, immobilization and higher-resolution imaging methods are necessary. While several methods have been developed that allow for long-term imaging of individual *C. elegans* animals, these methods utilize a "catch and release" strategy that limits temporal resolution and is better suited for events occurring on a developmental timescale (e.g., Guo *et al.*, 2008; Keil *et al.*, 2017) or rely on high-speed image acquisitions that can accommodate animal movement, but which limit spatial resolution (e.g., Gritti *et al.*, 2016). To image subcellular events that occur on a timescale of seconds to minutes, continuous immobilization is necessary. Continuous immobilization involves treatment with anesthetics and/or physical compression or confinement (Sulston and Horvitz, 1977; Chai *et al.*, 2012; Kim *et al.*, 2013; Hwang *et al.*, 2014; Luke *et al.*, 2014; Burnett *et al.*, 2018), which likely limit the duration of physiologically relevant image acquisition. Recently, an elegant system was described that allows for continuous image acquisition, under seemingly physiological conditions (Berger *et al.*, 2018); however, this method relies on a fairly sophisticated microfluidic device, and residual small-scale movement, such as pharyngeal pumping, may complicate automated monitoring of subcellular events.

We have previously described a simple mounting method that allows for high spatiotemporal imaging of mitosis in larval and adult GSCs (Gerhold *et al.*, 2015). Here, we systematically investigated the technical factors that might impact GSC mitosis in order to define near-physiological imaging conditions. We found that GSCs are sensitive to illumination intensity, anesthetic dose, and physical compression and discuss imaging parameters to minimize these effects. We further determined that preventing food intake is the major contributor to changes in GSC cell division during live imaging and define a window of image acquisition, from the start of sample preparation to the end of visualization, during which this effect appears negligible.

To capitalize on a key advantage of working with a model system such as *C. elegans*—the ability to conduct large-scale, population-based studies—we devised a generalizable computational strategy for spatial registration, tracking and automated pairing of mitotic centrosomes, which is robust for both unperturbed and atypical GSC mitoses and which can be adapted to other cell types and model systems. We use this method to explore how mitoses and mitotic features are distributed throughout the mitotic zone and to characterize GSC mitotic spindle orientation dynamics. Our optimized live-imaging conditions and largely automated image analysis enable large-scale studies of mitosis in vivo, in a highly tractable model system, facilitating the exploration of gene function within the *C. elegans* germline and, potentially, in other such complex tissues.

RESULTS AND DISCUSSION

A simple mounting method for intravital imaging of GSC mitosis does not affect viability or fertility

Traditional mounting methods to immobilize *C. elegans* involve compressing the animal between an agarose pad and coverslip, with or without the addition of paralytic drugs, such as sodium azide or tetramisole (Sulston and Horvitz, 1977; Chai *et al.*, 2012; Fang-Yen *et al.*, 2012). The use of agarose pads micropatterned with grooves, which approximate animal width, can constrain the worm's typical sinusoidal body movement, thereby reducing the need for anesthetics, while also ensuring an optimal and reproducible body position (Zhang *et al.*, 2008; Bourdages *et al.*, 2014; Gerhold *et al.*, 2015; Rivera Gomez and Schvarzstein, 2018). This method has the further advantage of being easy and inexpensive to implement and being suitable for use with a wide range of imaging platforms.

Our specific protocol uses a silicon wafer etched to produce several longitudinal, sloped ridges, approximately 26 μm tall and 50 μm wide, at the base, which is then used to create grooves of similar proportions in a 3% agarose pad (Figure 1A). Worms are mounted in a minimal salt buffer (M9) supplemented with 0.04% tetramisole, gently positioned within grooves using a mouth pipette, and compressed slightly by the addition of a coverslip. While this method has been used to image *C. elegans* adults (Gerhold *et al.*, 2015), here we focus primarily on animals in the late L4 larval stage of development. Animals mounted in this manner, and imaged for 40 min, showed no difference in survival or brood size when compared with controls (Figure 1, B and C). Thus, unlike longer-term immobilization and/or higher doses of tetramisole, which can impair viability (Chai *et al.*, 2012; Kim *et al.*, 2013; Burnett *et al.*, 2018), fertility, or other physiological readouts, such as motility (Dong *et al.*, 2018), our approach has a seemingly negligible impact on viability and germline function.

Cell cycle perturbations are observed in GSCs subjected to live imaging

To monitor GSC mitosis, we use *C. elegans* strains that express a fluorescently tagged version of β-tubulin under the control of germline-specific regulatory sequences, combined with a second marker to follow other structures of interest, such as histone H2B to visualize chromatin movement (strain JDU19: GFP::β-tubulin, mCH::Histone; Figure 1D) or actomyosin contractility regulators like ANI-1 and CCM-3 to facilitate gonad axis determination (strains UM679: mCH::β-tubulin; mNG::ANI-1 and ARG16: mCH:β-tubulin; CCM-3::mNG, respectively). We then track centrosome pairs, measure the distance between them in three dimensions (3D) (hereafter "spindle length"), and use reproducible changes in spindle length to define various mitotic landmarks, including nuclear envelope breakdown (NEBD) and anaphase onset (Figure 1, D and E; Gerhold *et al.*, 2015). To diagnose the state of GSCs during live imaging, we took advantage of the fact that cells must generally satisfy cell cycle checkpoints to undergo proper division. We assessed two checkpoints: the G2/M checkpoint, which prevents mitotic entry in response to DNA damage, stress signaling, and dietary conditions

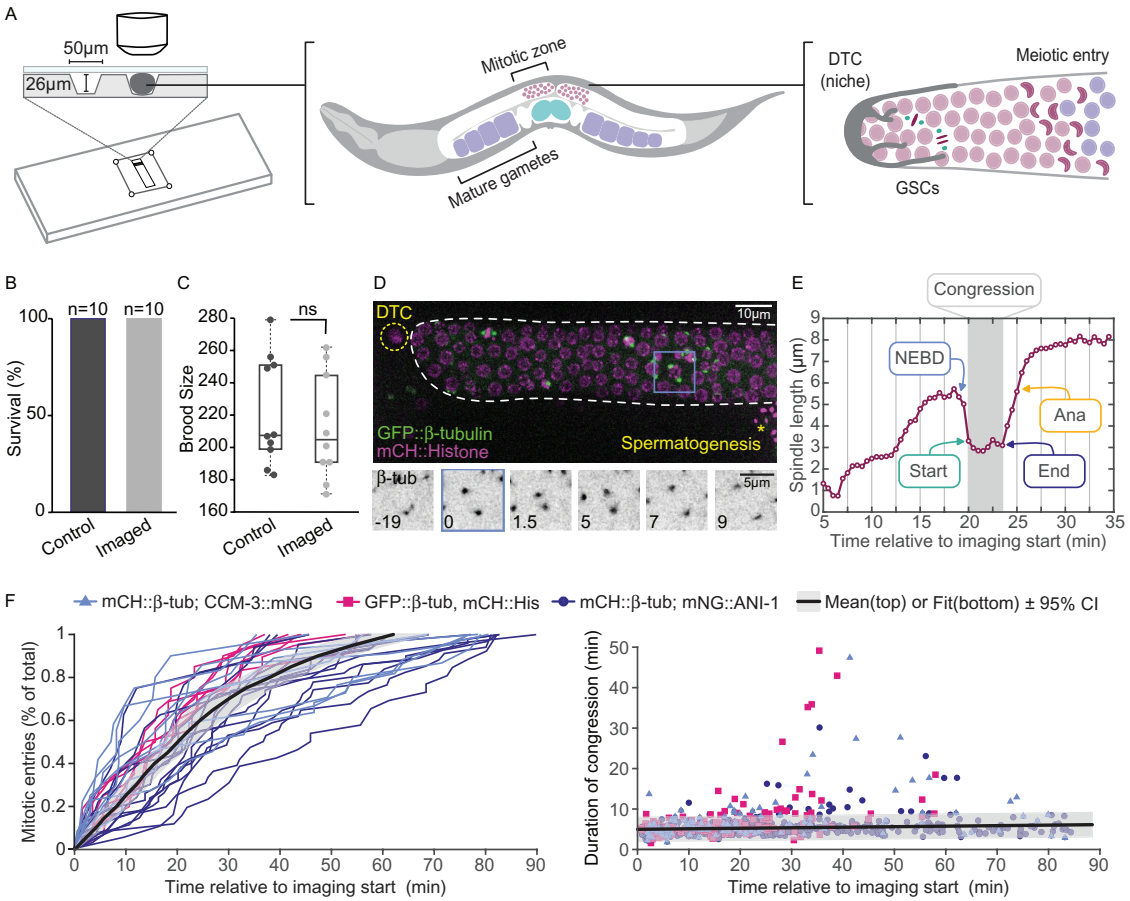

FIGURE 1: Cell cycle perturbations are observed in GSCs subjected to live imaging. (A) Schematic showing our mounting method for intravital imaging of *C. elegans* GSCs (left), the assembly line–like organization of the adult hermaphrodite germline (middle), and a close-up of the distal mitotic zone, with GSCs in association with their somatic niche, the DTC (right). (B, C) Percent survival (B) and total brood count (C) of individual animals (strain UM679: mCH::β-tubulin; mNG::ANI-1) that were left untreated (control) or imaged for 40 min (imaged) and recovered from the slide. Individual data points in C represent animals, box edges are the 25th and 75th percentiles, and whiskers extend to the farthest data points. ns = not significant ($p \geq 0.05$; two-tailed Student's *t* test). (D) Maximum intensity projection (top) of the distal gonad from a late L4 animal expressing GFP::β-tubulin (green) and mCH::Histone H2B (magenta; strain JDU19). The mitotic zone of the distal gonad is outlined in white, the nucleus of the DTC is outlined in yellow, and spermatogenesis, in the proximal gonad arm, is indicated by an asterisk. Single time points showing a maximum intensity projection of the GFP::β-tubulin signal for the blue boxed cell are shown below. Time is in minutes relative to NEBD. (E) Sample plot of centrosome-to-centrosome distance (spindle length) over time for a single GSC showing the stereotypic changes in spindle length used to identify NEBD, the start and end of congression and anaphase. (F) Mitotic entries as a percent of the total number of mitoses (left; each line represents data for a single gonad) and the duration of congression (right; each point represents a single GSC) over the course of 90-min-long image acquisitions, relative to image acquisition start. Data for three strains (JDU19: GFP::β-tubulin, mCH::Histone [magenta], $n = 140$ mitotic entries, 139 complete congressions; UM679: mCH::β-tubulin; mNG::ANI-1 [purple], $n = 339$ mitotic entries, 346 complete congressions; ARG16: mCH::β-tubulin; CCM-3::mNG [blue], $n = 129$ mitotic entries, 122 complete congressions) are shown. The mean (left) or the best fit (top; $y = 0.013x + 4.98$; $r = 0.17$, $p = 5.1879\text{e-}05$) is shown in black, with the 95% confidence interval for each shaded in gray.

(Rieder, 2011; Ables *et al.*, 2012), and the spindle assembly checkpoint (SAC), which delays anaphase onset and mitotic exit in the presence of unattached kinetochores, the multiprotein structure responsible for connecting chromosomes to spindle microtubules (London and Biggins, 2014).

We considered NEBD as the definitive sign of mitotic entry and satisfaction of the G2/M checkpoint and anaphase onset as an indication that cells had satisfied the SAC. To determine how long cells took to satisfy the SAC, we measured the duration of congression, which we define as the period of time after NEBD, once spindle length reaches a constant minimum, until the start of anaphase pole separation (Figure 1E; Gerhold *et al.*, 2015). Over the course of 90-min image acquisitions, we found that the number of cells entering mitosis decreased substantially, such that more than 80% of mitotic entries occurred within the first 40 min of imaging and almost none was observed after 60 min (Figure 1F). Further, we observed a weak, but significant, relationship between the start of congression, relative to the start of image acquisition, and the duration of congression, with a slight increase in the duration of congression over the 90-min imaging period (Figure 1F). We conclude that GSCs are sensitive to our imaging/mounting regime, with the overwhelming effect being a decrease in the number of mitotic entries, suggesting

that the cell cycle arrests at or before the G2/M checkpoint. Importantly, these results suggest that, under commonly used animal mounting conditions, there is a limited time window for physiologically relevant imaging of GSC mitosis.

Food deprivation is the primary factor impacting GSCs during live imaging

During mounting and live imaging, *C. elegans* animals are exposed to several potentially deleterious factors. These include laser exposure, treatment with paralytic drugs, physical compression, submergence in an aqueous buffer, and removal from a source of food and/or prevention of food intake due to paralysis (i.e., starvation; Figure 2A). As these factors are common to many mounting/imaging methods, we sought to explore how each contributes to changes in GSC cell cycle progression. As the average number of mitotic entries per animal and the average duration of congression showed the most pronounced changes after 40–50 min of imaging (Supplemental Figure S1A), we investigated the impact of different imaging/mounting factors over a 40-min period. We took animals that were continuously mounted and imaged for 90 min and divided the cells into two bins: those that divided between 0 and 40 min of imaging and those that divided between 40 and 80 min of imaging. We then compared cells in the second bin to cells from animals subjected to the following four treatments for 40 min, before being imaged for a further 40 min: 1) fully mounted, but not imaged; 2) anesthetized in aqueous buffer (M9 with 0.04% tetramisole), but not mounted or imaged; 3) submerged in aqueous buffer (M9 alone), but not anesthetized, mounted, or imaged; and 4) transferred to a normal feeding plate without a food source, that is, starved, but not submerged, anesthetized, mounted, or imaged (Figure 2B). Following all four treatments, we found that the number of mitotic entries was decreased and the duration of congression was increased, relative to cells in the first bin (0–40 min of imaging) and to an extent similar to what we observed in cells in the second bin (40–80 min of imaging). Thus removing animals from food is sufficient to produce the changes in GSC mitosis that we observe under continuous imaging conditions, suggesting that starvation is the principal perturbing factor for GSC cell cycle progression under our mounting/imaging regime.

GSCs are sensitive to laser exposure, anesthetic dose, mounting substrate, and temperature

To further investigate the impact of our mounting/imaging conditions on GSCs, we varied each factor individually to determine whether they could effect changes in GSC cell cycle progression. Effective spatial resolution is linked to the signal-to-noise ratio of an imaged specimen (Stelzer, 1998), and while increasing sample illumination may improve the signal-to-noise ratio, this often leads to phototoxicity in living samples (Dixit and Cyr, 2003). Thus the photosensitivity of GSCs must be considered when designing and interpreting live-imaging experiments. Similarly, the impact of paralytic agents used to immobilize worms and thus facilitate high-resolution imaging must also be assessed. Tetramisole is a cholinergic inhibitor commonly used for immobilizing *C. elegans* (Thienpont *et al.*, 1966; Aceves *et al.*, 1970; Lewis *et al.*, 1987), but its effect on GSCs has not been determined.

To test how light intensity affects GSCs, we increased the intensity of both excitation lasers by three- or sixfold, relative to our standard conditions, which use the minimum laser power necessary to visualize centrosomes in one channel and a second structure of interest in the other. To reduce light exposure, we imaged GSCs using only a single laser (561 nm), visualizing centrosomes alone. While neither increasing nor reducing laser exposure affected the number of mitotic entries, the duration of congression was significantly longer and more variable when laser intensity was increased (Figure 2C). To test whether the dose of tetramisole impacts dividing GSCs, we increased the concentration by 2.5- and 10-fold (0.1 and 0.4%, respectively) relative to the minimal concentration required to effectively immobilize worms for imaging (0.04%). We found that while increasing the concentration of tetramisole did not significantly affect the number of cells entering mitosis, a 10-fold increase led to significantly longer durations of congression (Figure 2C). Thus, both laser exposure and tetramisole dose can affect GSC mitosis, largely by delaying anaphase onset; however, visualization of GSCs is possible at laser intensity settings and tetramisole doses well below the threshold at which deleterious mitotic effects are observed.

Many methods for mounting *C. elegans* animals use a relatively rigid agarose pad, which can immobilize the worm via compression after a coverslip has been applied (Dong *et al.*, 2018). The use of micropatterned grooves that approximate animal size likely decreases this compression. Our mounting method makes use of an intermediate agarose concentration (3%), which preserves the integrity of the grooves without being overly rigid. To test whether agarose rigidity and/or compression impacts GSCs, we imaged animals on 10% agarose pads, with and without micropatterned grooves. In worms mounted on 10% agarose pads without grooves, we observed a trend toward fewer mitotic entries and longer durations of congression (Figure 2C). While neither trend was significant compared with control ($p = 0.0825$ and 0.094, respectively), the duration of congression was more variable under these conditions and the frequency of overly delayed cells was higher, with 21% of cells displaying a duration of congression greater than the 95th percentile value for controls. These results suggest that physical compression of the animal may perturb GSC divisions and is not an optimal mounting strategy. Notably, the mitotic parameters of GSCs imaged in animals mounted on 10% agarose pads with grooves were similar to those in animals mounted using our standard method (Figure 2C). This suggests that agarose micropatterning reduces the negative impact of physical compression and allows for more physiologically accurate observations of GSC divisions.

While grooves were typically made using custom-microfabricated silicon wafers, we also tested the effect of agarose micropatterning using vinyl long-play (LP) records, as described previously (Zhang *et al.*, 2008; Rivera Gomez and Schvarzstein, 2018). We found that mounting animals on 3% agarose pads molded with grooves from a vinyl record yielded reasonably good results, with similar numbers of mitotic entries per worm. However, we observed a slight, but significant, increase in the average duration of congression, when compared with our silicon wafers (Supplemental Figure S1B), similar to that which we observed in animals mounted on 10% agarose pads without grooves (Figure 2C). Thus LP-molded grooves can serve as an inexpensive and readily available alternative to micropatterned silicon wafers for GSC live imaging but likely do not preserve worm physiology as well as custom-fabricated molds.

Finally, *C. elegans* is generally maintained in the lab within a temperature range of 15–25°C, and most imaging experiments are conducted at "room temperature." However, room temperature can vary widely and may not be an accurate reflection of the actual temperature experienced by the sample during imaging. To assess the impact of temperature on GSC mitosis, we imaged animals at 15, 20, and 25°C, using a microfluidic temperature control device (CherryTemp) to maintain our samples at a stable temperature. While the number of mitotic entries appeared to be relatively constant across

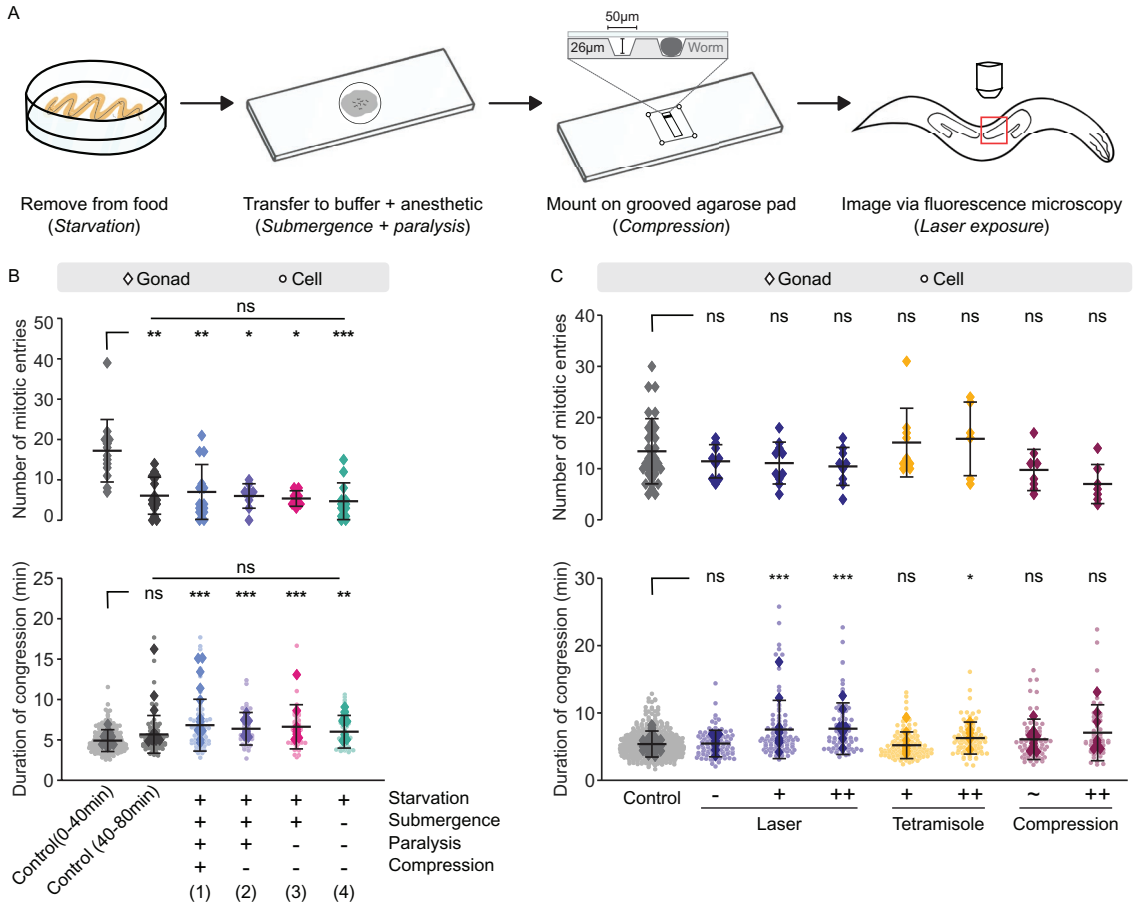

FIGURE 2: GSCs are sensitive to mounting and imaging conditions, with food deprivation being the most deleterious. (A) Schematic representation of the required steps for mounting animals and imaging GSC mitosis, with the potentially deleterious factors indicated in italics. (B) Beeswarm plots showing the number of GSCs entering mitosis per gonad (top) and the per cell and per gonad mean duration of congression (bottom) for animals subjected to the indicated four treatments for 40 min, before imaging for 40 min (blue, purple, magenta, and green), as compared with animals imaged continuously for 90 min (control; gray; $n = 40$ animals). Control data were divided into 0–40 ($n = 213$ cells) and 40–80 ($n = 84$ cells) bins relative to image acquisition start. Only cells that entered mitosis (top) or underwent a complete congression (bottom) within each bin were included (i.e., cells that started congression in the 0–40 min bin and ended congression in the 40–80 min bin were excluded). Blue = (1) fully mounted ($n = 14$ animals, 82 cells); purple = (2) anesthetized in aqueous buffer (M9 with 0.04% tetramisole), but not mounted ($n = 9$ animals, 48 cells); magenta = (3) submerged in aqueous buffer (M9 alone), but not anesthetized or mounted ($n = 8$ animals, 48 cells); and green = (4) starved, but not submerged, anesthetized or mounted ($n = 13$ animals, 48 cells). (C) Beeswarm plots as in B for animals imaged for 40 min under standard conditions (gray; $n = 32$ animals, 396 cells), when laser intensity was modified (purple) by a three- or sixfold increase (+ and ++; $n = 10$ animals, 94 cells; and $n = 9$ animals, 78 cells, respectively) or by eliminating the 488 laser (–; $n = 9$ animals, 99 cells) when the tetramisole dose was increased (yellow) by 2.5-fold (+; $n = 9$ animals, 125 cells) or 10-fold (++; $n = 6$ animals, 88 cells) or when the mounting substrate was modified (magenta) by increasing the agarose concentration to 10% with (~; $n = 8$ animals, 73 cells) or without (++; $n = 7$ animals, 48 cells) grooves. In B and C, black bars show the mean of the per animal (top) and per cell (bottom) values; error bars represent the SD. ns = not significant, $p \geq 0.05$; * = $p < 0.05$; ** = $p < 0.01$; *** = $p < 0.001$ by a Kruskal Wallis with a Tukey Kramer post hoc test. In B, p values reflect the comparison to control (0–40 min). All other comparisons were not significant. In C, p values reflect the comparison to control. All experiments were performed using strain UM679 (mCH::β-tubulin; mNG::ANI-1). For all panels, per gonad means are represented by diamonds and per cell values by circles.

temperatures, GSCs from animals imaged at 15°C had significantly longer durations of congression (Supplemental Figure S1C), suggesting that temperature is an additional factor that ought to be considered when live imaging GSCs.

In sum, we find that mitotic entry and exit in GSCs are sensitive to an array of factors that are commonly used in mounting and imaging *C. elegans* animals. However, minimally perturbing conditions can be found to afford high spatiotemporal live imaging suitable for mitotic studies. Our results indicate that food removal is the main factor to consider when live-imaging GSCs, providing further evidence that cell cycle progression in GSCs is highly responsive to dietary conditions (Hubbard *et al.*, 2013; Gerhold *et al.*, 2015; Seidel and Kimble, 2015). Importantly, our analysis defines a window of roughly 40 min, post–food removal, during which GSC physiology, at least with respect to mitosis, is minimally perturbed. As a typical M phase (prophase through late anaphase/telophase) in GSCs is

less than 30 min (mean ± SD = 27.6 ± 7.3 min; n = 138 cells) and congression is less than 6 min (mean ± SD = 5.4 ± 1.9 min; n = 396 cells), this window affords ample opportunity to observe multiple key mitotic events.

CentTracker enables automated monitoring and analysis of GSC mitosis

To follow GSC mitosis, we track individual centrosomes in 3D and manually pair centrosomes that belong to the same cell. Tracking and pairing is performed using the open-source platform TrackMate in Fiji (Schindelin *et al.*, 2012; Tinevez *et al.*, 2017). We then export the *x-y-z-t* coordinates of paired centrosomes into MATLAB, which permits rapid plotting and user-scoring of intercentrosome distance (spindle length) versus time graphs and automated extraction of mitotic features. Manual track curation and pairing is time- and labor-intensive, and large-scale analyses, such as genetic screens, are not realistic using this approach. Tracking is time-consuming largely because residual, global animal movement can mask individual centrosome movement (Supplemental Figure S2), leading to a high frequency of tracking errors. Furthermore, centrosome pairing requires visual assessment and manual labeling of each putative pair. To address these challenges, we constructed CentTracker, a largely automated analysis pipeline, based around a series of integrated modules (Figure 3A).

We reasoned that correcting for sample movement would permit the generation of sufficiently error-free tracks in TrackMate, such that automated pairing would be feasible. Thus the first CentTracker module was built to perform accurate image registration. Image registration, in this case, is a nontrivial problem due to the lack of reliable landmarks in our images and the fact that our labeled objects (centrosomes) are themselves highly dynamic. We based our registration approach on the observation that, while individual centrosomes are dynamic, the position of the metaphase plate (i.e., the spindle midpoint) is relatively stable with respect to the animal and/or germline. Moreover, the spindle midpoint is readily visible and thus easily marked. As the majority of animal movement occurs within the *x-y* plane, spindle midpoint marking can be performed on 2D maximum intensity z-projections, which further simplifies this step. The *x-y-t* coordinates of spindle midpoints are then used to generate a translation matrix by calculating midpoint displacement between adjacent time points. Applying this translation matrix effectively corrected for animal movement over time and was sufficient to constrain centrosome trajectories to a significantly smaller range (Figure 3A), such that the remaining centrosome movement was associated with bona fide spindle assembly dynamics (Supplemental Figure S2). This reduction in global movement also enables the identification of relevant tissue landmarks at a single time point, which can then be accurately propagated throughout the image acquisition. For *C. elegans* GSCs, we specified the distal tip and the distal–proximal axis of each gonad arm, which allowed us to position cells along the length of the mitotic zone relative to the distal end or niche (see Figure 4A).

Registered images are passed to TrackMate for spot (i.e., centrosome) detection and tracking (CentTracker Module 2). While image registration enhanced tracking accuracy, the low signal-to-noise ratio can lead to imperfect spot detection, which, in turn, can lead to spurious and/or incomplete tracks. In addition, GSC mitoses are often clustered (see Figure 4, C and D) such that two centrosomes from neighboring cells may be closer to one another than to their true pair, and spindle characteristics may vary, particularly when spindle formation is perturbed, which can confound accurate pairing using hard filtering criteria. To address these issues, we built a trainable track pair classifier (CentTracker Module 3) that uses a modified random forest algorithm (Pedregosa *et al.*, 2011) and a standard machine learning routine. Briefly, a data-refining set of crude filters are applied to spot and track descriptors taken from TrackMate (or any other tracking software) and then an algorithm classifies each possible pair of centrosome tracks as "true" or "false" pairs, based on 11 numerical features. The user provides training material to this algorithm, which allows the classifier to refine the relative weight of each parameter and generate a model that can be applied to unseen data (see Supplemental Methods).

Once a set of paired tracks has been generated, the coordinates of paired centrosomes, plus any additional, user-defined landmarks (e.g., the position of the gonadal distal tip) are passed to MATLAB (CentTracker Module 4). After data import, spindle length versus time graphs are presented to the user, which allows for rapid scoring of mitotic events (e.g., NEBD and anaphase onset) by simply clicking on the plot at the relevant position in time. In addition, if a graph is ambiguous, the user can call a time-lapse image, cropped and centered on the centrosome pair in question, for visual confirmation (Figure 3A).

To test the performance of CentTracker, we applied it to a subset of our previous, manually tracked data (Figure 3B; 10 animals, 205 true centrosome pairs, representing GSCs in various stages of mitosis, 131 of which undergo complete congression, that is, in which both NEBD and anaphase onset were captured) and evaluated two metrics: precision and discovery rate. We define "precision" as the percent of true centrosome pairs identified by CentTracker (i.e., true positives/[true positives + false positives]) and "discovery rate" as the number of cells identified by CentTracker that undergo a complete congression, relative to the number found using the manual method. CentTracker identified 164 centrosome pairs, 155 of which were validated as true pairs, for a precision of 94.5%, with a discovery rate of 82.4% (108/131 cells with complete congression). We next asked whether the performance of CentTracker could be improved further by removing residual tracking errors. To do so, we manually corrected for tracking errors in TrackMate, which were most commonly due to track truncations and/or breaks and spot misassignments, and supplied CentTracker with "error-free" tracked files. In this case, precision was unchanged (94.5%), but the discovery rate improved (113/131, 86.25%). Thus, compared with labor-intensive manual tracking, CentTracker identifies the majority (155/205, 75.6%) of true centrosome pairs with high precision, including a proportional number of cells that undergo a complete congression (63.9% vs. 69.6% of true pairs, manual vs. CentTracker, respectively). Persistent tracking errors account for a tolerable loss (<4%) in the discovery rate. Importantly, several features of mitosis, including duration of congression and spindle length, were similarly distributed when comparing cells identified using manual versus CentTracker pairing (Figure 3B), indicating that CentTracker is not biased for a certain subset of the population.

While CentTracker performed well on an unseen control data set, we wished to determine whether it would be robust enough to detect cells with aberrant mitoses. To this end, we challenged CentTracker with aberrantly short GSC mitoses (*mdf-2/Mad2(tm2190)* mutants; Gerhold *et al.*, 2015), delayed GSC mitoses (sixfold increase in laser intensity, this work), and severely perturbed spindle stability and delayed mitoses (*him-10/Nuf2*(RNAi) animals; Gerhold *et al.*, 2015). CentTracker performed well for aberrantly short and delayed mitoses (precision: 92 and 90.2%; discovery rate: 77.5 and 67.6%, respectively), but struggled when faced with cells with severe spindle perturbations (*him-10/Nuf2*(RNAi); precision: 79.3%; discovery rate: 38.8%; Figure 3B). Correcting for tracking errors before

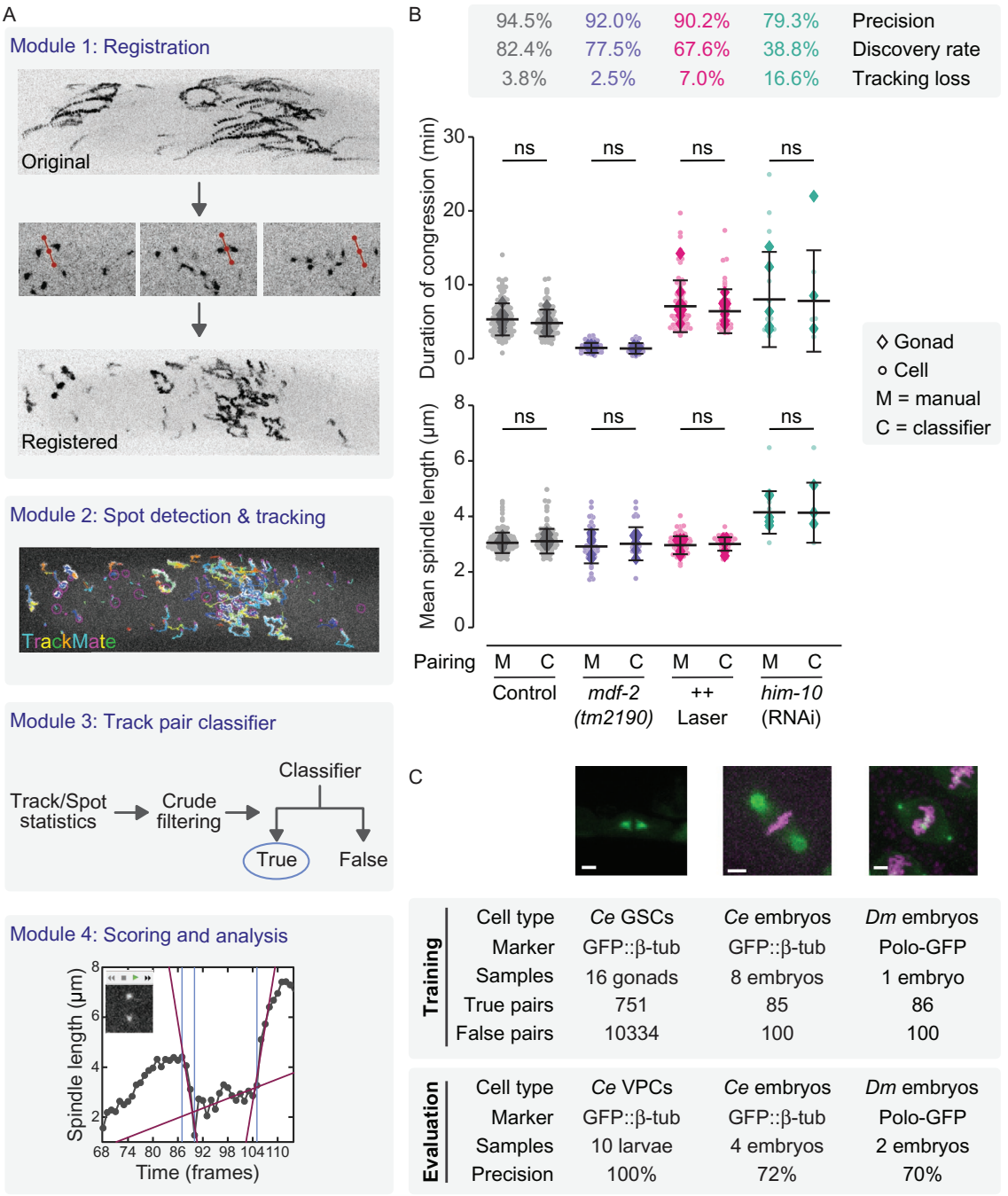

Training	Cell type	*Ce* GSCs	*Ce* embryos	*Dm* embryos
	Marker	GFP::β-tub	GFP::β-tub	Polo-GFP
	Samples	16 gonads	8 embryos	1 embryo
	True pairs	751	85	86
	False pairs	10334	100	100

Evaluation	Cell type	*Ce* VPCs	*Ce* embryos	*Dm* embryos
	Marker	GFP::β-tub	GFP::β-tub	Polo-GFP
	Samples	10 larvae	4 embryos	2 embryos
	Precision	100%	72%	70%

FIGURE 3: CentTracker enables automated monitoring of GSC mitosis. (A) Schematic overview of CentTracker workflow showing the tasks performed by each module. See the main text for details. (B) Comparative analysis of the duration of congression (top) and mean spindle length (bottom) for centrosome pairs assigned manually (M) or using the CentTracker classifier (C), in phenotypically wild-type animals (gray; mCH::β-tubulin; mNG::ANI-1; $n = 10$ animals, manual ground truth $n = 131$ cells, classifier $n = 108$ cells) and in animals mutant for *mdf-2* (purple; *mdf-2(tm2190)*; GFP::β-tubulin; $n = 6$ animals, manual ground truth $n = 40$ cells, classifier $n = 31$ cells), imaged with a sixfold increase in laser intensity (magenta; mCH::β-tubulin; mNG::ANI-1; $n = 9$ animals, manual ground truth $n = 71$ cells, classifier $n = 48$ cells) or depleted for HIM-10/Nuf2 (green; GFP::β-tubulin; *him-10*(RNAi); $n = 5$ animals, manual ground truth $n = 18$ cells, classifier $n = 7$ cells). Circles represent individual cells. Diamonds represent the mean per animal. Black bars show the mean of the per cell values; error bars represent the SD. Pairwise, manual vs. classifier, comparisons were performed using a two-tailed Student's *t* test, except for *him-10*(RNAi), where a Wilcoxon rank sum test was used. ns = not significant ($p \leq 0.05$). CentTracker's precision (true-positive rate), discovery rate (identified cells with complete congression as a percent of ground truth), and tracking loss (change in the number of identified cells with complete congression upon presenting the classifier with "error-free" tracks, as a percent of ground truth) for each condition is at the top. (C) Representative images (top) and summary tables for the training (middle) and evaluation (bottom) of CentTracker for pairing centrosomes in *C. elegans* (*Ce*) VPCs (left), *C. elegans* embryonic blastomeres (center), and *Drosophila* (*Dm*) syncytial embryos (right), using the indicated marker to track centrosomes. Scale bars = 3 µm.

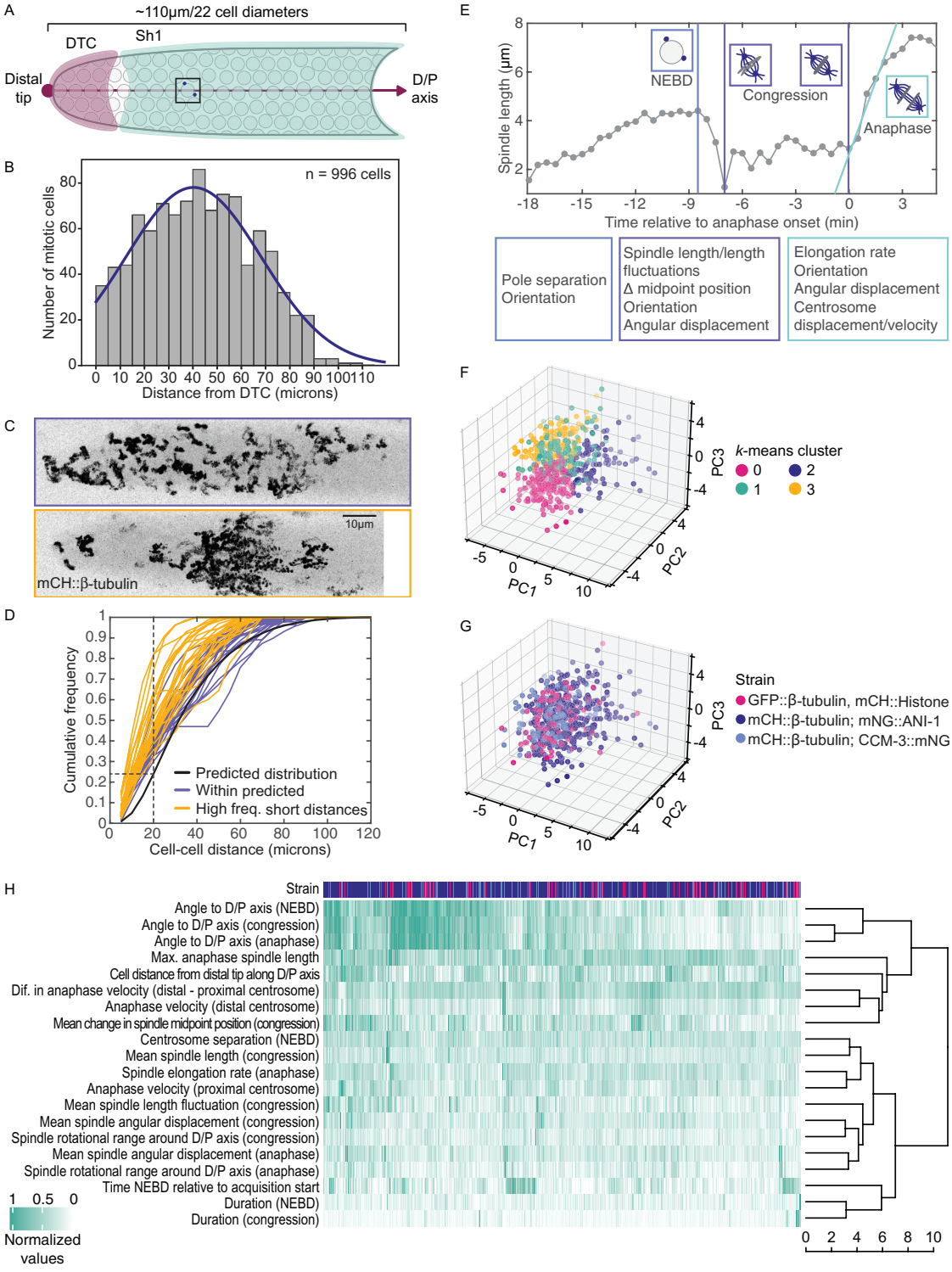

FIGURE 4: The spatial distribution of GSC mitoses is nonrandom but mitotic features do not identify distinct subpopulations of cells. (A) Schematic representation of the mitotic region of a late L4. Image registration in CentTracker allows for the distal tip (magenta circle) and distal–proximal (D/P) axis (magenta line) to be marked once and propagated through all time points. The DTC is in magenta; the Sh1 sheath cell is in green. (B) Histogram showing the number of GSC mitoses along the D/P axis, relative to the distal tip, in 5 µm/~1-cell-diameter bins. Gray bars represent the total number of mitoses for each bin. Purple line shows the normal distribution fit. Mean ± SD = 40.25 ± 28.07 µm. *n* = 996 cells from 74 animals. (C) Representative images of time- and z-maximum intensity projections of mCH::β-tubulin from a gonad with a uniform (top) compared to clustered (bottom) distribution of divisions. Scale bar = 10 µm. (D) The two-point correlation function for 46 gonads, with ≥10 mitotic cells, plotted as the cumulative frequency of mitotic cell-to-cell distances. The black line represents the mean predicted outcome, if mitoses were normally distributed along the D/P axis according to the Gaussian fit in B, but otherwise randomly

pairing led to a moderate increase in the number of informative cells found in these animals (discovery rate = 55%, corresponding to a 16.6% tracking loss). In all cases, mitotic features (duration of congression and spindle length) were similarly distributed in data sets generated by CentTracker versus those generated manually (Figure 3B). Thus, even in animals with perturbed mitoses, CentTracker can produce a relatively unbiased sampling of the underlying population, which should be sufficient to detect interesting phenotypes.

Finally, to test the generalizability of the CentTracker software, we applied it to several other cell types (Figure 3C). First, we used CentTracker to identify centrosome pairs in *C. elegans* larval vulval precursor cells (VPCs) in which centrosomes were also marked with β-tubulin::GFP. In this case, we did not have a large enough data set to train a new model; however, even using the classifier trained on mitotic GSCs, CentTracker was able to identify 55% of dividing VPCs with 100% precision. To test the "trainability" of CentTracker, we trained our classifier on *C. elegans* embryos, in which centrosomes were labeled with β-tubulin::GFP, and *Drosophila* embryos, in which centrosomes were marked with a GFP-tagged version of Polo kinase (Moutinho-Santos *et al.*, 1999; Archambault *et al.*, 2008). In both cases, even though the model was trained on a relatively small data set (85/100 and 86/100 true/false pairs, respectively) and centrosome detection and tracking were not optimized, the software identified true centrosome pairs in unseen data with 72% and 70% precision, respectively. Thus, CentTracker can be used to pair marked centrosomes in a range of mitotic cell types, even with suboptimal centrosome markers, such as Polo kinase, which is also strongly recruited to kinetochores and the midbody (Moutinho-Santos *et al.*, 1999; Archambault *et al.*, 2008).

GSC divisions are not randomly distributed along the length of the mitotic zone in L4 larvae

We next took advantage of CentTracker to collect data for a large population of mitotic GSCs (n = 996 cells; 74 animals, three genotypes/strains) and used this data set to ask how different aspects of mitosis were distributed across the GSC population. We first assessed the spatial distribution of GSC divisions within the mitotic zone (Figure 4A). We found that the frequency of divisions along the gonadal distal–proximal (D/P) axis followed a roughly normal distribution, with fewer divisions in the distal-most region, a peak in mitoses approximately eight cell diameters (40 μm) from the distal tip, and very few divisions in the most proximal region of the mitotic zone (Figure 4B). Thus, the frequency of divisions in late L4 larval germlines follows a pattern similar to that which has been observed in adults (Hansen *et al.*, 2004; Crittenden *et al.*, 2006; Maciejowski *et al.*, 2006; Gordon *et al.*, 2020). Anecdotally, we observed that GSC divisions tended to be clustered together within the same germline. To determine whether our data supported this, we calculated the distribution of pair-wise distances between dividing cells, using the two-point correlation function (TPCF), in all germlines with at least 10 divisions (n = 46 animals; 821 cells; three genotypes/strains). We found that the majority of germlines (24/46) had a cumulative distribution of mitotic cell-to-cell distances that differed significantly from that predicted by our observed normal distribution of division frequency alone (Figure 4, C and D). Further, most germlines (37/46) displayed a higher than expected frequency of short mitotic cell-to-cell distances (≤20 μm or four cell diameters) and a subset of germlines showed a clear step-like TPCF, suggesting at least two discrete clusters, separated by a zone devoid of divisions (unpublished data). Interestingly, analysis of fixed adult germlines has also suggested spatial clustering of GSC mitoses (Maciejowski *et al.*, 2006), although the reasons for this are poorly understood. Thus, GSC mitoses are not randomly arrayed within the mitotic zone and show both a peak in frequency at intermediate distances from the distal tip and a tendency to occur within close proximity to one another.

Mitotic properties do not identify discrete populations within the GSC pool

We next asked whether these spatial heterogeneities were accompanied by any population-level patterns in mitotic dynamics. We extracted a variety of mitotic features, including the duration of congression, centrosome positioning at NEBD, spindle length and length fluctuations, spindle rotation and orientation relative to the D/P axis, individual centrosome velocities, and spindle elongation rates (Figure 4, A and E, Supplemental Table S1). To visualize cell-to-cell similarities in the GSC population, we performed principal component analysis (PCA) across 34 defined mitotic features (Figure 4F). PCA is a common dimensionality reduction tool that identifies axes of maximal variance (principal components [PCs]) within multidimensional data. Plotting observations along these new axes can accentuate differences within the population and, when combined with a clustering algorithm (here *k*-means), identify subpopulations with a common collection of features. PCA was carried out on the subset of cells for which we were able to extract values for all mitotic parameters (n = 547). We found that less than 50% of the variance within our GSC population could be explained by the first three PCs (Supplemental Figure S3A), and plotting all cells along these PC axes did not reveal any obvious subpopulations. *k*-means clustering analysis suggested an optimum cluster number of four; however, the predicted clusters are not well separated (Figure 4F and Supplemental Figure S3B). Together, these results suggest that GSCs do not form natural clusters based on the mitotic parameters extracted and that covariance between features is minimal. Importantly, neither genotype (Figure 4G), the time of mitotic entry relative to the start of imaging (Supplemental Figure S3C), nor the position of a cell along the D/P axis (Supplemental Figure S3D) was predictive of a cell's position within PC space.

To investigate potential correlations between mitotic features while preserving feature identity, we generated heat maps for each

positioned. Distributions within the predicted outcome ($p > 0.05$) are in purple, those that differ significantly from it ($p \leq 0.05$; two-sample Kolmogorov–Smirnov test) are in yellow. Dashed lines highlight the increased frequency of short (≤20 μm) mitotic cell-to-cell distances in most gonads. (E) Representative spindle length vs. time (relative to anaphase onset) plot for a single cell showing mitotic landmarks and the types of mitotic features extracted for different mitotic stages (NEBD, congression and anaphase). (F, G) The results of PCA using 34 mitotic features, followed by *k*-means clustering. A set of 547 GSCs are plotted along the first three principle components and are color-coded by cluster assignment (F) or by strain of origin (G). (H) Heat map showing the normalized values for the subset of mitotic features listed on the left, measured for dividing GSCs from each strain of origin (top, with color coding as in G) and ordered by hierarchical clustering, with the linkage between clusters indicated by the dendrogram to the right. Dendrogram branch length represents the Euclidean distance between clusters.

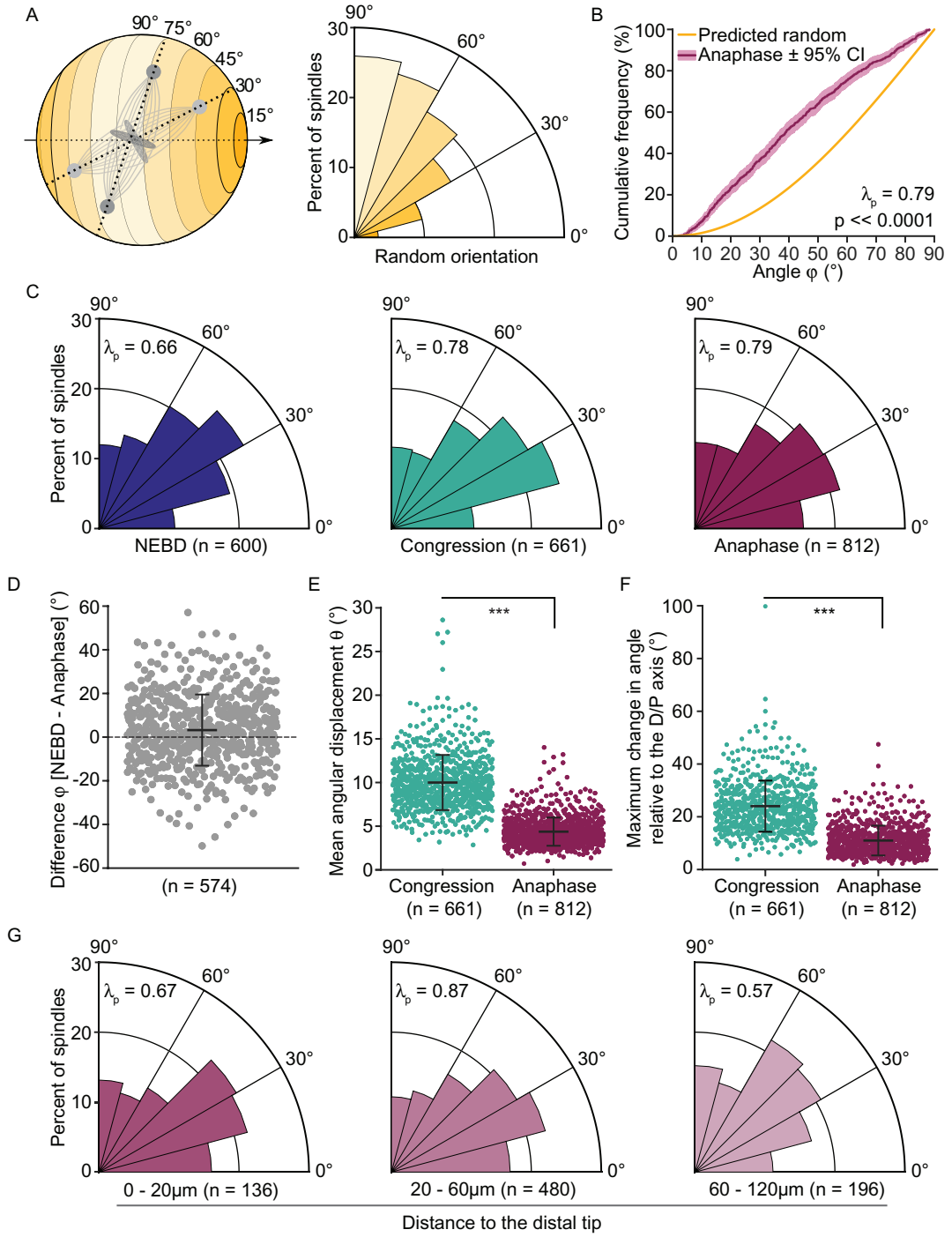

FIGURE 5: GSC spindles preferentially orient along the gonadal D/P axis in L4 larvae. (A) Schematic representation (left) of a cell modeled as a sphere, with the D/P axis (black, dashed, arrowed line) running through the sphere's center. The cortical surface sampled by centrosomes is shaded according to spindle angle, from parallel (0°; dark yellow) to orthogonal (90°; pale yellow). Spindles at 30° (light gray) and at 75° (dark gray) relative to the D/P axis are shown. The polar histogram (right) shows the predicted distribution of spindle angles if orientation were random with respect to the D/P Axis. (B) The cumulative distribution for spindle angles relative to the D/P axis for the calculated random distribution (yellow line) and the measured angles at anaphase (magenta line, mean with 95% confidence interval shaded, $n = 812$ spindles). Measured angles are biased towards the D/P axis ($p = 2 \times 10^{-61}$, one-sample Kolmogorov–Smirnov test). (C) Polar histograms showing the bias in spindle orientation, during NEBD (purple, left), congression (green, middle) and anaphase (magenta, right). The distributions are similar at all three points ($p > 0.05$; two-sample Kolmogorov–Smirnov test). (D) Beeswarm plot showing the net change (per cell) in spindle angle, relative to the D/P axis, from NEBD to anaphase. (Mean ± SD = 3.2 ± 16.3° is greater than 0, indicating that spindles are more aligned with the D/P axis at anaphase ($n = 574$ spindles; $p < 0.001$ by a one-sample Student's t test). (E, F) Beeswarm plots showing the per cell, mean spindle angular displacement (E) and the maximum change in spindle angle relative to the D/P axis (F) during congression (green, $n = 661$; mean ± SD = 10.0 ± 3.2° [E] and 24.0 ± 9.7° [F]) and anaphase (magenta, $n = 812$;

feature and performed hierarchical clustering (Figure 4H and Supplemental Figure S3E). As expected, features derived from related measurements (e.g., centrosome displacement and velocity) clustered together (Supplemental Figure S3E). Notably, none of our assayed features, many of which might be expected to inform on spindle assembly and/or stability, correlated appreciably with the duration of congression (Figure 4H). Thus, while variation in the duration of congression in GSCs is SAC-dependent (Gerhold *et al.*, 2015), our analysis of mitotic features in GSCs undergoing unperturbed mitoses does not identify a specific aspect of spindle assembly that is strongly predictive of difficulties satisfying the SAC. Similarly, position along the D/P axis of the gonad did not correlate with any mitotic feature (Figure 4H), suggesting that spatial distinctions within the GSC population, which may potentially be related to "stemness" (Hubbard and Schedl, 2019), do not impact core mechanisms of mitotic progression.

Spindle orientation in GSCs is biased toward the gonadal D/P axis in L4 larvae

The most strongly correlated features within our data related to spindle orientation along the D/P axis of the gonad. We found that a cell's spindle orientation is similar throughout mitosis, from NEBD through anaphase, suggesting that spindles might be rotationally confined relative to the gonadal axis (Figure 4H). Regulated spindle orientation is an astral microtubule-dependent process that can shape tissues and impact stem cell fate (Yamashita *et al.*, 2003; Noatynska *et al.*, 2012; Kulukian and Fuchs, 2013). Spindle orientation in GSCs was proposed to be arbitrary with respect to the D/P axis (Kimble and Hirsh, 1979; Crittenden *et al.*, 2006), suggesting that regulated asymmetric divisions, which generate two intrinsically different daughter cells, do not contribute to stem cell maintenance and that GSCs are maintained as a population, with stem cell fate dictated by proximity to the niche (Morrison and Kimble, 2006). It has been shown recently, however, that spindle orientation in adult GSCs is biased at the interface of the DTC and proximal somatic sheath cell (Sh1), such that one daughter cell remains in contact with DTC (niche) appendages, while the other moves under the sheath cell and differentiates (Gordon *et al.*, 2020), suggesting that a subset of GSC divisions may be asymmetric. This boundary region, where the DTC and Sh1 meet, also corresponds to the peak zone of GSC mitoses. In late L4 larvae, the DTC-Sh1 interface is relatively smooth and orthogonal to the gonadal axis (Figure 4A; Gordon *et al.*, 2020), such that divisions biased along it will also be biased relative to the D/P axis.

To address whether spindle orientation in late L4 larvae showed any orientation biases, we measured the angle formed by each spindle and the gonadal D/P axis (Figure 4A). We assessed spindle orientation in 3D to capture the full range of spindle movements and to avoid potential pitfalls associated with 2D projected measurements (Jüschke *et al.*, 2014). We compared our measurements to the theoretical distribution for random orientation along the gonadal axis, using a model described by Jüschke *et al.*, wherein the probability of a spindle assuming a particular orientation is proportional to the surface area of the sphere at this angle and bias along a defined axis (here the D/P axis) is expressed by λ_p values greater than 0 (Figure 5A and see *Materials and Methods*; Jüschke *et al.*, 2014). Compared with this calculated random distribution, we found a strong enrichment of spindles that were oriented toward the D/P axis and a pronounced lack of spindles in the orthogonal orientation ($\lambda_p = 0.79$; Figure 5, B and C). As predicted by our hierarchical clustering analysis (Figure 4H), this orientation bias was observed throughout mitosis, that is, at NEBD, during congression and in anaphase (Figure 5C).

We see a similar bias in spindle orientation at NEBD and anaphase at a population level (Figure 5C) and a relatively strong correlation between these two values on a per cell basis ($r = 0.75$, $p << 0.001$), suggesting that anaphase spindle orientation, relative to the D/P axis, is generally prefigured by centrosome positioning before NEBD. However, we also found that, on average, spindles tended to skew toward the D/P axis as GSCs progressed from NEBD to anaphase (mean = 3.2°; Figure 5D) and that, at least in some cells, significant changes in spindle orientation could occur between these two events (StDev = 16.3°; max = 57°; Figure 5D). Thus changes in spindle orientation can occur between NEBD and anaphase, with the end result that spindles, on average, adopt an orientation more parallel to the D/P axis by anaphase.

Spindle movements (such as rotation) are typically achieved by cortical forces that are applied on astral microtubules and that can cause spindle oscillations, with an amplitude correlating with force magnitude (Grill and Hyman, 2005; Pecreaux *et al.*, 2006). To determine whether GSC spindles undergo oscillations, we measured the change in spindle angle between time points (angular displacement), during congression and anaphase. We found that angular displacement was significantly greater during congression than during anaphase (Figure 5E) and the maximum rotational range relative to the D/P axis was also much broader (Figure 5F). Thus spindle orientation relative to the D/P axis is largely set by the start of anaphase, after which rotational movements are minimal. The fact that spindles tend to oscillate more around their midpoint during congression than in anaphase suggests that the loss of cohesion between sister chromatids may stabilize the net force applied on astral microtubules during anaphase. We also observed that the pair-wise oscillatory movements of the two centrosomes were nearly equal during congression (average difference in displacement between the two centrosomes: 0.1 ± 0.1 μm). This is different from what is observed in the asymmetrically dividing one-cell *C. elegans* embryo, where force imbalance results in a significantly greater oscillatory movement of the posterior centrosome compared with the anterior one (Grill *et al.*, 2003; Pécréaux *et al.*, 2016). This result suggests that forces are largely balanced on each side of the spindle during congression and is compatible with the notion that GSC divisions are symmetric.

Finally, we asked whether anaphase spindle orientation, which is predictive of daughter cell positioning after cytokinesis, varied

mean ± SD = 4.4 ± 1.6° [E] and 11.0 ± 5.7° [F]). Spindles are less dynamic during anaphase by both metrics (*** $p < 0.001$; paired-sample Student's *t* test). In D–F, black bars represent the mean and error bars show the SD. (G) Polar histograms showing the distribution of spindle angles, relative to the D/P axis, binned by distance from the gonad's distal tip. Bin edges and *n* are given underneath. The distributions of angles are similar in all bins ($p > 0.05$; two-sample Kolmogorov–Smirnov test), except for the most proximal, 60–120 μm, bin, which is significantly different from the middle, 20–60 μm, bin ($p = 0.012$; two-sample Kolmogorov–Smirnov test). In C and G, $\lambda_p > 0$ indicates a horizontal (i.e., toward the D/P axis) enrichment in spindle orientation (see *Materials and Methods*), which is statistically different from random ($p < 0.01$; one-sample Kolmogorov–Smirnov test).

along the length of the gonad. To test this, we used our measured distribution of mitotic entries along the mitotic zone and published reports on the position of the DTC and the DTC-Sh1 interface in late L4 larvae to define three bins: GSCs mainly dividing under the DTC cap (0–20 µm, covering approximately four cell diameters from the distal tip; Crittenden *et al*., 2006), GSCs near the DTC-Sh1 interface (20–60 µm, comprising the zone of peak GSC mitosis, that we see at ~40 µm or eight cell diameters; Gordon *et al*., 2020), and GSCs dividing in a region covered by Sh1 only (60–120 µm, extending to the transition zone, ~22–24 cell diameters from the distal tip; Crittenden *et al*., 2006; Gordon *et al*., 2020). We found that anaphase spindle orientation in each of these three regions is statistically different from the calculated random distribution and is significantly more biased toward the D/P axis (Figure 5G), although this bias is less pronounced for spindles in GSCs within the Sh1-only, most proximal region of the mitotic zone. These results indicate that spindle orientation in GSCs in late L4 larvae is generally oriented toward the D/P axis in all regions of the gonad and does not appear to be strongly influenced by the DTC-Sh1 interface.

Previous reports have inferred that spindle orientation in adults is unbiased relative to the gonadal D/P axis (Kimble and Hirsh, 1979; Crittenden *et al*., 2006; Gordon *et al*., 2020); however, spindle angles were not assessed in 3D and the absence of an orientation bias was not specifically tested. To test whether our results were specific to L4 larval germlines, we measured spindle orientation in 1 day-old adults ($n = 147$ cells in 19 animals) using the same methodology as for L4 larvae. We found that spindles were also biased toward the D/P axis in these animals ($\lambda_p = 0.49$), although to a lesser extent than in L4 larvae (Supplemental Figure S4C). Similarly to L4 larvae, we also found that the bias in spindle orientation in adults was consistent along the length of the mitotic zone, in the distalmost region under the DTC cap, in the region of peak mitoses and approximate DTC-Sh1 interface and in the more proximal, predicted Sh1-only region (Supplemental Figure S4, B and D). We note that our measurements are similar to a recent report (mean angle to the D/P axis ± SD = 46.9 ± 21.8°; Supplemental Figure S4C, vs. 42.5 ± 24.7°; Gordon *et al*., 2020; $p = 0.13$, by a two-sample Kolmogorov–Smirnov test), suggesting that biases in GSC spindle orientation relative to the D/P axis are widespread but may have been overlooked, further underscoring the value of 3D analysis and comparison to a theoretical random distribution (Jüschke *et al*., 2014).

Altogether our results suggest that, in larvae and adults, GSCs tend to divide along the D/P axis. In larval GSCs, this bias in orientation is not accompanied by evidence of regulated asymmetric cell division, in terms of spindle dynamics or relevant landmarks. One possibility is that underlying anisotropies in cell and/or tissue shape contribute to GSC spindle orientation, but further study is needed to address this. We further do not exclude the possibility that the general bias toward D/P-oriented divisions in adult gonads may be further refined by additional tissue features, such as the precise shape of the DTC-Sh1 interface (Gordon *et al*., 2020), which we did not assess here.

In sum, this work provides the first systematic analysis of technical factors that affect the division of *C. elegans* GSCs in live-imaging experiments. While animal starvation is the main technical factor impacting GSC mitosis, our work demonstrates that its effects are minimal within the first 40 min of acquisition, providing a window during which GSCs division can be visualized under seemingly physiological conditions. We further introduce CentTracker as a flexible image analysis pipeline that facilitates the extraction of GSC mitotic features from large-scale imaging data sets and that is adaptable for analyses of other cell types and other organisms. Finally, we use CentTracker to analyze several features of GSC mitosis, providing evidence for spatial clustering of GSC divisions and a penetrant bias in spindle orientation toward the D/P axis of the gonad.

MATERIALS AND METHODS

Request a protocol through *Bio-protocol*.

C. elegans strains and culture

C. elegans animals were maintained at 20°C on nematode growth medium (NGM) and fed with *Escherichia coli* strain OP50 according to standard protocols (Brenner, 1974). Synchronized L1 larvae were obtained by collecting gravid hermaphrodites and dissolving them in a solution of 1.2% sodium hypochlorite and 250 mM sodium hydroxide. Embryos were collected, washed in M9 buffer (22.04 mM KH_2PO_4, 42.27 mM Na_2HPO_4, 85.55 mM NaCl, 1 mM $MgSO_4$), and allowed to hatch for 24 h at 15°C in M9 buffer. Late L4 larvae were obtained by inoculation of synchronized L1 larvae on NGM plates containing 1 mM isopropyl β-D-thiogalactoside (IPTG) and 25 µg/ml carbenicillin (Carb) and fed for 44–48 h with *E. coli* strain HT115 transformed with the empty RNA interference (RNAi) control vector L4440. Consistent with previous reports (Chaudhari *et al*., 2016), we find that animals reared on HT115 bacteria have a more uniformly high frequency of GSC divisions (unpublished data).

Strains imaged for this study were UM679: *ltSi567[pOD1517/pSW222; Pmex-5::mCherry::tbb-2::tbb-2_3′UTR; cb-unc-119(+)]I; ani-1(mon7[mNeonGreen^3xFlag::ani-1]) III*, ARG16: *ltSi567[pOD1517/pSW222; Pmex-5::mCherry::tbb-2::tbb-2_3′UTR; cb-unc-119(+)]I; ccm-3(mon9[ccm-3::mNeonGreen^3xFlag]) II; unc-119(ed3) III*, and JDU19: *ijmSi7 [pJD348/pSW077; mosI_5′mex-5_GFP::tbb-2; mCherry::his-11; cb-unc-119(+)]I; unc-119(ed3) III*.

Worm mounting and live imaging

Animals were anesthetized in M9 buffer containing 0.04% tetramisole (Sigma) and transferred to a 3% agarose pad, molded with grooves made by a custom microfabricated silica plate, onto which a coverslip was placed, as described (Gerhold *et al*., 2015). The chamber was backfilled with M9 buffer containing 0.04% tetramisole and sealed using VaLaP (1:1:1 Vaseline, lanolin, and paraffin). Images (except those in Supplemental Figure S1A; see Supplemental Methods) were acquired at room temperature (~20°C) with an AxioCam 506 Mono camera (Zeiss) mounted on an inverted Cell Observer spinning-disk confocal microscope (Zeiss; Yokogawa), using a 60× Plan Apochromat DIC (UV) VIS-IR oil immersion objective (Zeiss), controlled by Zen software (Zeiss). Acquisitions used 200 ms exposure with 488 nm (35 mW) and 561 nm (50 mW) solid-state lasers, both set at 10% of intensity. Confocal sections, with a 0.5 µm z-step, were acquired over 38 µm of depth, at 30 s intervals, for durations of 40 or 90 min.

Survival and brood size assays

Imaged animals were recovered by gently lifting the coverslip and removing the animal by mouth pipette. The animals were washed several times in M9 buffer before being transferred to individual seeded NGM plates. Survival was assessed by monitoring animal movement a few hours after the transfer. The animals were transferred to fresh plates every 24 h for a total of 72 h, and brood size was determined by counting the progeny present on each plate 48 h after the animal had been removed.

Manual GSC centrosome tracking and pairing

Centrosome identification and tracking were performed using the Laplacian of the Gaussian (LoG) blob detector, with an estimated

blob diameter of 2.5 µm, and linear assignment problem (LAP) spot linker, with linking and gap-closing max distances of 2.7 µm and a gap-closing max frame of 2 in the Fiji plug-in TrackMate (Schindelin *et al*., 2012; Tinevez *et al*., 2017). We note that these parameters will vary depending on centrosome marker, image quality, and cell type and should be optimized according to the experiment. Tracks were manually curated to correct for tracking errors (centrosome misassignments were corrected, and broken tracks were joined, but gaps in a single-centrosome tracks were generally tolerated), and all spots within a given centrosome track were renamed to indicate association between appropriate pairs (centrosomes within the same cell; e.g., Cent1a and Cent1b). Track curation was performed within TrackMate, using built-in functionalities.

Scoring GSC mitotic events from pairs of tracked centrosomes

Centrosome *x*-*y*-*z*-*t* coordinates and labels were exported and analyzed using a custom MATLAB script. The centrosome-to-centrosome distance (spindle length) was plotted relative to time (frames), and graphs were used to define three mitotic events: NEBD (the last frame before the rapid decrease in spindle length, which is coincident with the appearance of microtubules within the nuclear space and thus NEBD), the start of chromosome congression (the first frame, post-NEBD, at which spindle length reaches a stable minimum), and anaphase onset (the last frame before rapid spindle elongation). Mitotic events were scored manually, by clicking on spindle length versus frame plots, with the option of calling a cropped time-lapse image of the cell in question for visual confirmation. The duration of congression was calculated from the points of intersection of three least-squares lines fitted to (1) spindle length from four frames before and including the start of congression, (2) all frames between the start of congression and anaphase onset, and (3) four frames, including the end of congression and the three following frames. All subsequent data analysis was performed using these mitotic events as landmarks to align cells and calculate various mitotic features. To calculate the total duration of mitosis (M phase) in GSCs, we used spindle length versus time plots and measured the amount of time between the start of spindle pole separation (prophase) and the end of spindle elongation (late anaphase/early telophase) in all cells for which complete mitoses were captured.

CentTracker workflow

The workflow for CentTracker involves four steps: registration, tracking, track pairing, and cell scoring (Figure 3A). To correct for sample movement in the *x*-*y* plane (registration; Module 1), we generate a z-maximum intensity projection of the time-lapse image and manually mark the approximate position of the metaphase plate in a single cell, or set of cells, by drawing a line orthogonal to the spindle axis. To facilitate this process and to avoid the potentially confounding effect of spindle orientation in the *z*-plane, we generally select isolated cells that are oriented within the imaging (i.e., *x*-*y*) plane. This step uses a set of ImageJ macros, which automate all steps aside from spindle midpoint marking. An *x*-*y*-*t* translation matrix for registration is constructed by calculating a 2D direction vector for each time point $v_t = p_{t-1} - p_t$, where p_t and p_{t-1} are midpoint positions of the same spindle at time points t and $t - 1$, respectively. To combine translation matrices from different spindles, matrices are concatenated by time axis. Input movies are then registered by shifting all z-slices of time t by the direction vector v_t and zero-padding the margins. Translation matrix generation and image registration are performed in Python. Spot detection and track construction (Module 2) are performed by TrackMate (Tinevez *et al*., 2017), as in the manual method (described above) but excluding the spot labeling and track curation steps. We note, however, that any spot detection and tracking paradigm could be used, as long as the output data are compatible with the track pairer (Module 3). Track pairing (Module 3) is performed using a trainable, machine-learning–based approach, which is implemented in Python using scikit-learn (Pedregosa *et al*., 2011). Crude filters (the minimum duration of individual track pairs, the minimum number of frames in which two tracks coappear, and the maximum distance between two tracks at any frame) are applied to the data, and the resulting, curated data set is converted into a set of 11 numerical features, which are fed into a random forest classifier to generate true/false predictions. Model details are provided in the Supplemental Methods. The *x*-*y*-*z*-*t* coordinates of paired centrosomes are passed to MATLAB and analyzed as for manual pairs, using custom scripts (described above). Step-by-step instructions, examples, and software code/scripts are available to download in a GitHub repository (https://github.com/yifnzhao/CentTracker). The main modules of the CentTracker were developed using Python 3.8.5. Existing packages and software are used whenever possible. The essential Python libraries used in the CentTracker software include numpy (van der Walt *et al*., 2011), pandas (McKinney, 2011), scikit-learn (Pedregosa *et al*., 2011), and scikit-image (van der Walt *et al*., 2014).

CentTracker data sets

The control data set consists of GSCs from a total of 16 individuals from strains UM679 and JDU19, imaged for 40 or 90 min for this article. We used the control data set to train, validate, and evaluate the random forest models in CentTracker. We then evaluated the generalization ability of CentTracker on three unseen *C. elegans* GSC data sets with different degrees of perturbation: we used previously published image data from our labs for (Gerhold *et al*., 2015) GSCs in *mdf-2*(*tm2190*) and *him-10*(RNAi) animals (Ahringer RNAi collection, clone sjj_R12B2.4; Kamath *et al*., 2003) and data from control animals imaged with a sixfold increase in laser intensity (this work). We further applied CentTracker to three additional, previously acquired image data sets from different tissues and/or model systems: *C. elegans* VPCs and embryos (A.R.G., unpublished data) and *Drosophila melanogaster* embryos (V. Archambault, unpublished data).

Definition of the D/P gonadal axis

The distal tip (D) was defined in 3D as the distal-most point of the gonad, at the center-most z-slice of the image (i.e., the *xy*-plane that passes through the middle of the rachis for the majority of the mitotic zone). The D/P axis (α) was then defined as a straight line from the distal tip (D) along the middle of the tissue (rachis) toward the proximal region (P). The vector α representing the distal–proximal axis was assumed to be constant across time points and was calculated as:

$$\alpha = \left(xD - xP,\ yD - yP,\ zD - zP\right)$$

Animals with distorted (e.g., curved) sections of the gonad were excluded.

Spindle orientation measurements in 3D

Spindle orientation calculations were carried out in MATLAB unless otherwise noted. The spindle was represented as a vector c connecting the 3D coordinates (x, y, z) of the two centrosomes (*C1*, *C2*) at each time point of a registered movie:

$$c = (xC1 - xC2,\ yC1 - yC2,\ zC1 - zC2)$$

The orientation of the spindle relative to the D/P axis was defined as the angle ϕ measured between the vector c and the vector α, representing the distal–proximal axis of the gonad (as described above). ϕ was calculated at each time point using the following scalar product, where II II represents the vector's norm:

$$\phi = \arccos \frac{c \cdot \alpha}{\|c\| \cdot \|\alpha\|}$$

The change in mitotic spindle orientation between time points (angular displacement) was defined as the angle Θ measured between the vector c_t connecting the two centrosomes at a given time point and that connecting the same centrosomes at the next time point (c_{t+1}). It was calculated at each time point using the following scalar product, where II II represents the vector's norm:

$$\theta = arcos \frac{c_t \cdot c_{t+1}}{\|c_t\| \cdot \|c_{t+1}\|}$$

The theoretical random distribution of spindle angles to the D/P axis was calculated by adapting a method described previously (Jüschke *et al.*, 2014), in which the probability of spindle poles orienting at a given angle is proportional to the surface area of a sphere at this angle. A GSC was approximated as a sphere of radius 1 that is traversed in its center by a straight line defining the distal–proximal (0°) axis. The angle ϕ formed by the intersection of the spindle and D/P axes defined a cortical circumference (C):

$$C = 2\pi \sin \phi$$

The surface area of the sphere $A\phi$ found between the D/P axis (0°) and the cortical circumference of a given angle (ϕ) and its symmetric counterpart ($-\phi$, where $0° \le \phi \le 90°$) can be calculated as

$$A\phi = \int_{-\phi}^{\phi} 2\pi \sin a\, da = -4\pi \cos \phi$$

The fraction $f\phi$ of the cortical surface area within this angle ($A\phi$) to the total surface area of the sphere ($A90° = 4\pi$) can be determined as

$$f\phi = \frac{-4\pi \cos \phi}{4\pi} = -\cos \phi$$

If mitotic spindle orientation were randomly distributed between parallel (0°) and perpendicular (90°) to the D/P axis, the probability P of a spindle orientation found between two given angles (ϕ_1 and ϕ_2, where $0° \le \phi_1 < \phi_2 \le 90°$) can be calculated as

$$P = f\phi_2 - f\ \phi_1 = -\cos\ \phi_2 + \cos\ \phi_1$$

The deviation of measured GSC spindle orientation from the calculated theoretical random distribution (λ_p) was determined using the R fit parameter script, as previously described (Jüschke *et al.*, 2014). Briefly, the λ_p value reports the degree of horizontal enrichment (i.e., parallel to the D/P axis) of GSC spindle angles, with a λ_p value of 0 indicating no particular orientation bias and a λ_p value greater than 0 indicating bias. The value scales with the relative enrichment and, as reference, would equal ~6 if all 812 anaphase spindle angles were oriented parallel to the D/P axis. Orientation bias along an axis orthogonal to the D/P axis (λ_o) was 0 in all conditions, indicating that there is no specific orientation bias in this second axis. The hypothesis that GSC spindle orientation is random was tested against the calculated theoretical random distribution by a one-sample Kolmogorov–Smirnov test (MATLAB kstest). To test the hypotheses that GSC spindle orientation is the same with respect to the mitotic stage and the position along the D/P axis, we applied two-sample Kolmogorov–Smirnov tests (MATLAB kstest2) with Bonferroni corrections.

Spatial analysis of GSC divisions

To measure the frequency of mitotic GSCs as a function of distance along the D/P axis, the Euclidean distance in *x* for the mean spindle midpoint of each cell relative to the distal tip was calculated and the distribution was sorted into 24 bins in Python 3.8 using the JupyterLab environment and key libraries including numpy 1.18.5 (Harris *et al.*, 2020), pandas 1.0.5 (McKinney, 2011), and matplotlib 3.2.2 (Hunter, 2007). A Gaussian fit to the distribution was determined using a Levenberg–Marquardt algorithm and least-squares statistic, using the astropy package 4.0.1post1 (Astropy Collaboration *et al.*, 2018; Robitaille *et al.*, 2013). The two-point correlation function (TPCF) for each gonad was computed in MATLAB by calculating the Euclidean distance in *x-y-z* between each cell and every other cell in the same gonad, using the 3D coordinates of the spindle midpoint at anaphase onset as the cell's centroid. The resulting distances were binned by 5 µm, and bin counts were converted to a cumulative frequency distribution. To calculate the predicted TPCF, a random Gaussian distribution of 10,000 *x* coordinates, with parameters equal to the Gaussian fit for measured mitotic frequency along the D/P axis, and a random uniform distribution of 10,000 *y* and 10,000 *z* coordinates, confined within the maximum range for these values for all gonads, were generated. For each gonad, 10,000 TPCF calculations with *n* cells, where *n* = the number of measured mitotic cells, were performed, using random draws with replacement from simulated *x-y-z* coordinates to create mitotic cell centroids. The average of these 10,000 iterations was taken as the representative predicted TPCF for a given gonad and was compared with the measured TPCF using a two-sample Kolmogorov–Smirnov test (MATLAB kstest2). Gonads enriched for cell–cell distances ≤20 µm were defined as those for which the measured frequency was more than twice the SD for the simulated TPCF set.

Large-scale analysis of GSC mitotic features

Mitotic features were calculated and feature lists were compiled in MATLAB. PCA and *k*-means clustering were performed in Python using scikit-learn 0.22.1 (Pedregosa *et al.*, 2011), with the following modules: Data were standardized using sklearn.preprocessing.StandardScaler().fit_transform(); PCA was carried out using sklearn.decomposition.PCA(*n_components = 34, svd_solver = 'auto'*); *k*-means clustering was carried out using sklearn.cluster.KMeans(n_clusters = 4); Silhouette coefficient calculations and plots were performed using sklearn.metrics.silhouette_samples and sklearn.metrics.silhouette_score. Hierarchical clustering and heatmap generation were carried out using the R package ComplexHeatmap 2.4.3 (Gu *et al.*, 2016), using the complete linkage clustering method with Euclidean as the distance metric.

Additional statistical analysis

Curve fitting in Figure 1F was performed using the MATLAB Curve Fitting Toolbox. Outliers, as defined as cells with a duration of congression shorter or longer than 1.5× the interquartile range above the 75th quartile or below the 25th quartile, respectively, were excluded. Comparison between two independent samples was

performed using a two-tailed Student's *t* test (MATLAB ttest2) except for Figure 3B, *him-10*(RNAi), where a Wilcoxon rank sum test (MATLAB ranksum) was performed. Comparison of multiple means was performed using a Kruskal–Wallis test with a Tukey–Kramer post hoc test (MATLAB kruskalwallis and multcompare). Increased variability in the duration of congression (Figure 2C) was assessed by performing a Kruskal–Wallis test with a Tukey–Kramer post hoc test (MATLAB kruskalwallis and multcompare) on the distribution of sample residuals. If $p < 0.05$, we concluded that a treatment led to a more variable outcome.

ACKNOWLEDGMENTS

We are grateful to Vincent Archambault (Institute for Research in Immunology and Cancer, Université de Montréal [IRIC, UdeM]) for sharing unpublished movies of *Drosophila* syncytial embryos undergoing mitosis, as well as Amy Maddox (University of North Carolina, Chapel Hill) and Arshad Desai (University of California, San Diego) for sharing strains and reagents. We thank Christian Charboneau of IRIC's Bio-imaging facility and the staff at McGill's Advanced BioImaging Facility (ABIF) for technical assistance, members of the Hickson, FitzHarris, Labbé, and Gerhold labs for help and advice, Preshanth Jagannathan for advice on spatial clustering analysis and Sébastien Lemieux (IRIC, UdeM) for critical reading of the manuscript. R.M.Z. held an Alexander Graham Bell Canada Graduate Scholarship from the Natural Sciences and Engineering Research Council of Canada (NSERC), an IRIC Doctoral Scholarship, and scholarships from UdeM's molecular biology programs and the school of graduate and postdoctoral studies. Y. Z. was partially supported by the Sheila Ann MacInnis Grant Science Undergraduate Research Award (SURA). This work was funded by a grant from the Canadian Institutes of Health Research (MOP-115171) to J-C. L. and A.R.G. IRIC is supported in part by the Canadian Center for Excellence in Commercialization and Research, the Canada Foundation for Innovation, and the Fonds de Recherche du Québec—Santé. We also thank the reviewers for their constructive feedback.

REFERENCES

Ables ET, Laws KM, Drummond-Barbosa D (2012). Control of adult stem cells in vivo by a dynamic physiological environment: diet-dependent systemic factors in Drosophila and beyond. Wiley Interdiscip Rev Dev Biol 1, 657–674.

Aceves J, Erlij D, Martínez-Marañón R (1970). The mechanism of the paralysing action of tetramisole on Ascaris somatic muscle. Br J Pharmacol 38, 602–607.

Archambault V, D'Avino PP, Deery MJ, Lilley KS, Glover DM (2008). Sequestration of Polo kinase to microtubules by phosphopriming-independent binding to Map205 is relieved by phosphorylation at a CDK site in mitosis. Genes Dev 22, 2707–2720.

Astropy Collaboration, Price-Whelan AM, Sipőcz BM, Günther HM, Lim PL, Crawford SM, Conseil S, Shupe DL, Craig MW, Dencheva N, *et al.* (2018). The Astropy Project: Building an Open-science Project and Status of the v2.0 Core Package. Astrophys J 156, 123.

Berger S, Lattmann E, Aegerter-Wilmsen T, Hengartner M, Hajnal A, deMello A, Casadevall i Solvas X (2018). Long-term C. elegans immobilization enables high resolution developmental studies in vivo. Lab Chip 18, 1359–1368.

Bourdages KG, Lacroix B, Dorn JF, Descovich CP, Maddox AS (2014). Quantitative analysis of cytokinesis in situ during C. elegans postembryonic development. PLoS One 9, e110689.

Brenner S (1974). The genetics of Caenorhabditis elegans. Genetics 77, 71–94.

Burnett K, Edsinger E, Albrecht DR (2018). Rapid and gentle hydrogel encapsulation of living organisms enables long-term microscopy over multiple hours. Commu Biol 1, 73.

Chai Y, Li W, Feng G, Yang Y, Wang X, Ou G (2012). Live imaging of cellular dynamics during Caenorhabditis elegans postembryonic development. Nat Protoc 7, 2090–2102.

Chaudhari SN, Mukherjee M, Vagasi AS, Bi G, Rahman MM, Nguyen CQ, Paul L, Selhub J, Kipreos ET (2016). Bacterial folates provide an exogenous signal for C. elegans germline stem cell proliferation. Dev Cell 38, 33–46.

Crittenden SL, Leonhard KA, Byrd DT, Kimble J (2006). Cellular analyses of the mitotic region in the Caenorhabditis elegans adult germ line. Mol Biol Cell 17, 3051–3061.

Dixit R, Cyr R (2003). Cell damage and reactive oxygen species production induced by fluorescence microscopy: effect on mitosis and guidelines for non-invasive fluorescence microscopy. Plant J 36, 280–290.

Dong L, Cornaglia M, Krishnamani G, Zhang J, Mouchiroud L, Lehnert T, Auwerx J, Gijs MAM (2018). Reversible and long-term immobilization in a hydrogel-microbead matrix for high-resolution imaging of Caenorhabditis elegans and other small organisms. PLoS One 13, e0193989.

Fang-Yen C, Gabel CV, Samuel ADT, Bargmann CI, Avery L (2012). Laser microsurgery in Caenorhabditis elegans. Methods Cell Biol 107, 177–206.

Gerhold AR, Ryan J, Vallée-Trudeau J-N, Dorn JF, Labbé J-C, Maddox PS (2015). Investigating the regulation of stem and progenitor cell mitotic progression by in situ imaging. Curr Biol 25, 1123–1134.

Gordon KL, Zussman JW, Li X, Miller C, Sherwood DR (2020). Stem cell niche exit in C. elegans via orientation and segregation of daughter cells by a cryptic cell outside the niche. eLife 9, e56383.

Grill SW, Howard J, Schäffer E, Stelzer EH, Hyman AA (2003). The distribution of active force generators controls mitotic spindle position. Science 301, 518–521.

Grill SW, Hyman AA (2005). Spindle positioning by cortical pulling forces. Dev Cell 8, 461–465.

Gritti N, Kienle S, Filina O, van Zon JS (2016). Long-term time-lapse microscopy of C. elegans post-embryonic development. Nat Commun 7, 12500.

Gu Z, Eils R, Schlesner M (2016). Complex heatmaps reveal patterns and correlations in multidimensional genomic data. Bioinformatics 32, 2847–2849.

Guo SX, Bourgeois F, Chokshi T, Durr NJ, Hilliard MA, Chronis N, Ben-Yakar A (2008). Femtosecond laser nanoaxotomy lab-on-a-chip for in vivo nerve regeneration studies. Nat Methods 5, 531–533.

Hansen D, Albert Hubbard EJ, Schedl T (2004). Multi-pathway control of the proliferation versus meiotic development decision in the Caenorhabditis elegans germline. Dev Biol 268, 342–357.

Harris CR, Millman KJ, van der Walt SJ, Gommers R, Virtanen P, Cournapeau D, Wieser E, Taylor J, Berg S, Smith NJ, *et al.* (2020). Array programming with NumPy. Nature 585, 357–362.

Hubbard EJ, Korta DZ, Dalfó D (2013). Physiological control of germline development. Adv Exp Med Biol 757, 101–131.

Hubbard EJA, Schedl T (2019). Biology of the Caenorhabditis elegans germline stem cell system. Genetics 213, 1145–1188.

Hunter JD (2007). Matplotlib: a 2D graphics environment. Comput Sci Eng 9, 90–95.

Hwang H, Krajniak J, Matsunaga Y, Benian GM, Lu H (2014). On-demand optical immobilization of Caenorhabditis elegans for high-resolution imaging and microinjection. Lab Chip 14, 3498–3501.

Januschke J, Näthke I (2014). Stem cell decisions: a twist of fate or a niche market? Semin Cell Dev Biol 34, 116–123.

Joshi PM, Riddle MR, Djabrayan NJV, Rothman JH (2010). C. elegans as a model for stem cell biology. Dev Dyn 239, 1539–1554.

Jüschke C, Xie Y, Postiglione MP, Knoblich JA (2014). Analysis and modeling of mitotic spindle orientations in three dimensions. Proc Natl Acad Sci USA 111, 1014.

Kamath RS, Fraser AG, Dong Y, Poulin G, Durbin R, Gotta M, Kanapin A, Bot NL, Moreno S, Sohrmann M, *et al.* (2003). Systematic functional analysis of the Caenorhabditis elegans genome using RNAi. Nature 421, 231–237.

Keil W, Kutscher LM, Shaham S, Siggia ED (2017). Long-term high-resolution imaging of developing C. elegans larvae with microfluidics. Dev Cell 40, 202–214.

Kim E, Sun L, Gabel CV, Fang-Yen C (2013). Long-term imaging of Caenorhabditis elegans using nanoparticle-mediated immobilization. PLoS One 8, e53419.

Kimble J (1981). Alterations in cell lineage following laser ablation of cells in the somatic gonad of Caenorhabditis elegans. Dev Biol 87, 286–300.

Kimble J, Crittenden SL (2007). Controls of germline stem cells, entry into meiosis, and the sperm/oocyte decision in Caenorhabditis elegans. Annu Rev Cell Dev Biol 23, 405–433.

Kimble J, Hirsh D (1979). The postembryonic cell lineages of the hermaphrodite and male gonads in Caenorhabditis elegans. Dev Biol 70, 396–417.

Kimble JE, White JG (1981). On the control of germ cell development in Caenorhabditis elegans. Dev Biol 81, 208–219.
Kotak S (2019). Mechanisms of spindle positioning: lessons from worms and mammalian cells. Biomolecules 9, 80.
Kulukian A, Fuchs E (2013). Spindle orientation and epidermal morphogenesis. Philos Trans R Soc Lond B Biol Sci 368, 20130016.
Lewis JA, Fleming JT, McLafferty S, Murphy H, Wu C (1987). The levamisole receptor, a cholinergic receptor of the nematode Caenorhabditis elegans. Mol Pharmacol 31, 185–193.
London N, Biggins S (2014). Signalling dynamics in the spindle checkpoint response. Nat Rev Mol Cell Biol 15, 736–747.
Lu MS, Johnston CA (2013). Molecular pathways regulating mitotic spindle orientation in animal cells. Development 140, 1843–1856.
Luke CJ, Niehaus JZ, O'Reilly LP, Watkins SC (2014). Non-microfluidic methods for imaging live C. elegans. Methods 68, 542–547.
Maciejowski J, Ugel N, Mishra B, Isopi M, Hubbard EJA (2006). Quantitative analysis of germline mitosis in adult C. elegans. Dev Biol 292, 142–151.
McKinney W (2011). Pandas: a Foundational Python Library for Data Analysis and Statistics. Python High Perform Sci Comp, 10, 1–9.
Morrison SJ, Kimble J (2006). Asymmetric and symmetric stem-cell divisions in development and cancer. Nature 441, 1068–1074.
Moutinho-Santos T, Sampaio P, Amorim I, Costa M, Sunkel CE (1999). In vivo localisation of the mitotic POLO kinase shows a highly dynamic association with the mitotic apparatus during early embryogenesis in Drosophila. Biol Cell 91, 585–596.
Narbonne P, Gerhold AR, Maddox PS, Labbé J-C (2016). The C. elegans GSCs: s powerful model for in vivo study of adult stem cell regulation. Int J Stem Cell Res Ther 3, 044.
Noatynska A, Gotta M, Meraldi P (2012). Mitotic spindle (DIS)orientation and DISease: cause or consequence? J Cell Biol 199, 1025–1035.
Park S, Greco V, Cockburn K (2016). Live imaging of stem cells: answering old questions and raising new ones. Curr Opin Cell Biol 43, 30–37.
Pécréaux J, Redemann S, Alayan Z, Mercat B, Pastezeur S, Garzon-Coral C, Hyman AA, Howard J (2016). The mitotic spindle in the one-cell C. elegans embryo is positioned with high precision and stability. Biophys J 111, 1773–1784.
Pecreaux J, Röper JC, Kruse K, Jülicher F, Hyman AA, Grill SW, Howard J (2006). Spindle oscillations during asymmetric cell division require a threshold number of active cortical force generators. Curr Biol 16, 2111–2122.
Pedregosa F, Varoquaux G, Gramfort A, Michel V, Thirion B, Grisel O, Blondel M, Prettenhofer P, Weiss R, Dubourg V, *et al*. (2011). Scikit-learn: machine learning in Python. J Mach Learn Res 12, 2825–2830.
Rieder CL (2011). Mitosis in vertebrates: the G2/M and M/A transitions and their associated checkpoints. Chromosome Res 19, 291–306.
Rivera Gomez KA, Schvarzstein M (2018). Immobilization of nematodes for live imaging using an agarose pad produced with a vinyl record. MicroPubl Biol 2018, doi:10.17912/QG0J-VT85.
Robitaille TP, Tollerud EJ, Greenfield P, Droettboom M, Bray E, Aldcroft T, Davis M, Ginsburg A, Price-Whelan AM, Kerzendorf WE, *et al*. (2013). Astropy: a community Python package for astronomy. Astron Astrophys 558, A33.
Rosu S, Cohen-Fix O (2017). Live-imaging analysis of germ cell proliferation in the C. elegans adult supports a stochastic model for stem cell proliferation. Dev Biol 423, 93–100.
Schindelin J, Arganda-Carreras I, Frise E, Kaynig V, Longair M, Pietzsch T, Preibisch S, Rueden C, Saalfeld S, Schmid B, *et al*. (2012). Fiji: an open-source platform for biological-image analysis. Nat Methods 9, 676–682.
Schofield R (1978). The relationship between the spleen colony-forming cell and the haemopoietic stem cell. Blood Cells 4, 7–25.
Seidel HS, Kimble J (2015). Cell-cycle quiescence maintains Caenorhabditis elegans germline stem cells independent of GLP-1/Notch. eLife 4, e10832.
Stelzer (1998). Contrast, resolution, pixelation, dynamic range and signal-to-noise ratio: fundamental limits to resolution in fluorescence light microscopy. J Microsc 189, 15–24.
Sulston JE, Horvitz HR (1977). Post-embryonic cell lineages of the nematode, Caenorhabditis elegans. Dev Biol 56, 110–156.
Thienpont D, Vanparijs OF, Raeymaekers AH, Vandenberk J, Demoen JA, Allewijn FT, Marsboom RP, Niemegeers CJ, Schellekens KH, Janssen PA (1966). Tetramisole (R 8299), a new, potent broad spectrum anthelmintic. Nature 209, 1084–1086.
Tinevez J-Y, Perry N, Schindelin J, Hoopes GM, Reynolds GD, Laplantine E, Bednarek SY, Shorte SL, Eliceiri KW (2017). TrackMate: an open and extensible platform for single-particle tracking. Methods 115, 80–90.
van der Walt S, Colbert SC, Varoquaux G (2011). The NumPy array: a structure for efficient numerical computation. Comput Sci Eng 13, 22–30.
van der Walt S, Schönberger JL, Nunez-Iglesias J, Boulogne F, Warner JD, Yager N, Gouillart E, Yu T, the scikit-image contributors (2014). scikit-image: image processing in Python. PeerJ 2, e453.
Weaver BAA, Cleveland DW (2005). Decoding the links between mitosis, cancer, and chemotherapy: the mitotic checkpoint, adaptation, and cell death. Cancer Cell 8, 7–12.
Yamashita YM, Jones DL, Fuller MT (2003). Orientation of asymmetric stem cell division by the APC tumor suppressor and centrosome. Science 301, 1547.
Zhang M, Chung SH, Fang-Yen C, Craig C, Kerr RA, Suzuki H, Samuel ADT, Mazur E, Schafer WR (2008). A self-regulating feed-forward circuit controlling C. elegans egg-laying behavior. Curr Biol 18, 1445–1455.